Published in final edited form as:
J Am Chem Soc. 2013 March 20; 135(11): 4260–4272. doi:10.1021/ja308915x.

Correlation Between Structural, Spectroscopic, and Reactivity Properties Within a Series of Structurally Analogous Metastable Manganese(III)-Alkylperoxo Complexes

Michael K. Coggins[†], **Vlad Martin-Diaconescu**[‡], **Serena DeBeer**[‡,§], and **Julie A. Kovacs**[†]

[†]The Department of Chemistry, University of Washington, Box 351700, Seattle, Washington 98195-1700, United States

[‡]Max-Planck-Institute for Chemical Energy Conversion, Stiftstrasse 34-36, 45470 Mulheim an der Ruhr, Germany

[§]Department of Chemistry and Chemical Biology, Cornell University, Ithaca, New York 14853, United States

Abstract

Manganese–peroxos are proposed as key intermediates in a number of important biochemical and synthetic transformations. Our understanding of the structural, spectroscopic, and reactivity properties of these metastable species is limited, however, and correlations between these properties have yet to be established experimentally. Herein we report the crystallographic structures of a series of structurally related metastable Mn(III)–OOR compounds, and examine their spectroscopic and reactivity properties. The four reported Mn(III)–OOR compounds extend the number of known end-on Mn(III)–(η^1-peroxos) to six. The ligand backbone is shown to alter the metal–ligand distances and modulate the electronic properties key to bonding and activation of the peroxo. The mechanism of thermal decay of these metastable species is examined via variable-temperature kinetics. Strong correlations between structural (O–O and Mn···N^{py,quin} distances), spectroscopic (E(π_v*(O–O) → Mn CT band), $\nu_{O–O}$), and kinetic ($\Delta H^{\ddagger}$ and $\Delta S^{\ddagger}$) parameters for these complexes provide compelling evidence for rate-limiting O–O bond cleavage. Products identified in the final reaction mixtures of Mn(III)–OOR decay are consistent with homolytic O–O bond scission. The N-heterocyclic amines and ligand backbone (Et vs Pr) are found to modulate structural and reactivity properties, and O–O bond activation is shown, both experimentally and theoretically, to track with metal ion Lewis acidity. The peroxo O–O bond is shown to gradually become more activated as the N-heterocyclic amines move closer to the metal ion causing a decrease in π-donation from the peroxo π_v*(O–O) orbital. The reported work represents one of very few examples of experimentally verified relationships between structure and function.

Introduction

Manganese (Mn)-containing enzymes promote a number of important biochemical[1–14] and synthetic[15–19] transformations involving dioxygen and reduced derivatives thereof. Many of

Corresponding Author: kovacs@chem.washington.edu.

Supporting Information: Quantitative UV/vis of alkylperoxo **1a–4a** and titration between ^{t}BuOOH + five-coordinate 2, 3, ESI-MS and FT-IR of Mn–^{16}O^{16}O^{t}Bu and Mn–^{18}O^{18}O^{t}Bu compounds, plots showing correlation between structural, spectroscopic, and kinetic parameters, electronic spectra and Eyring plots associated with the thermal decay kinetics of alkylperoxo compounds **1a–4a**, and plots showing zero-order dependence on substrate concentration. This material is available free of charge via the Internet at http://pubs.acs.org.

Notes: The authors declare no competing financial interest.

these reactions, including two of the most fundamental processes of life, photosynthetic H_2O splitting[7,20] and DNA biosynthesis,[1] are proposed to involve Mn-peroxo intermediates. These peroxo intermediates form either en route to more reactive high-valent metal-oxo intermediates,[1,21,22] or as a result of O–O coupling.[7,23] Alkylperoxo Mn–OOR intermediates are proposed to play a key role in the reactions catalyzed by manganese lipoxygenase[3,18,24,25] and homoprotocatechuate 2,3-dioxygenase enzymes,[8,26,27] as well as in industrial pro-cesses.[16,28–31] With the exception of one system,[14] biological Mn–peroxo intermediates have yet to be observed. Our understanding of the structural and electronic properties that favor O–O bond formation vs O–O bond cleavage is extremely limited for Mn. This is because very few Mn– peroxos, biological or synthetic, have been characterized,[14,15,17,32–43] due in part to their thermal and photochemical instability. Of the six structurally characterized mononuclear Mn(III)–peroxos,[32,34,38,41–43] five contain the peroxo in a side-on (η^2) binding mode. The O–O bond distances associated with the Mn(III)–(η^2-peroxos) all fall within a fairly narrow range (1.403(4)–1.428(7) Å). Not surprisingly, the spectroscopic properties of these metastable species are also relatively invariant.[15,17,35,36,41–43] The only structural evidence for an end-on (η^1) peroxo binding mode with mononuclear manganese(III) is for an alkylperoxo compound.[32] The O–O bond in this end-on Mn(III)(η^1-alkylperoxo)[32] is significantly more activated (1.457(7) Å) than the side-on Mn(III)–(η^2-peroxos).[34,38,41–43] More examples of end-on Mn(III)(η^1-peroxo) compounds are needed, however, in order to establish a relationship between binding mode and levels of O–O bond activation. Ultimately, we wish to understand how structure influences reactivity and the factors that favor O–O vs Mn–O bond cleavage and formation.

Previously, we reported the first example of a Mn(III)– alkylperoxo complex, $[Mn^{III}(S^{Me2}N_4(QuinoEN))(OO^tBu)]$-$(BPh_4)$ (1a).[32] This complex is high-spin ($S = 2$) and intensely blue in color. A lower-resolution structure of an end-on cumenyl peroxo derivative, $[Mn^{III}(S^{Me2}N_4(QuinoEN))$-$(OOCm)](BPh_4)$, was also included. Preliminary evidence suggested that the thermal decomposition of these species proceeded via a mechanism involving homolytic O–O bond scission.[32] This reaction pathway was unprecedented with synthetic Mn–peroxos which are typically shown to undergo heterolytic O–O bond cleavage.[44] Our observations[32] further contrast with those made for high-spin Fe(III)–OOR complexes, which are shown to preferentially undergo Fe–O bond cleavage.[45–48] With synthetic Fe(III)–OOR complexes, a low-spin state is required in order for homolytic O–O bond cleavage to occur.[46,49] With end-on iron hydroperoxo intermediates proton-assisted heterolytic O–O bond cleavage has been shown to occur when the Fe(III)–OOH is low spin,[50,51] whereas heterolytic Fe–O bond cleavage occurs when the Fe(III)–OOH is high spin.[47]

Herein we report the synthesis as well as spectroscopic and structural characterization of a series of four new structurally related high-spin ($S = 2$) manganese(III)–alkylperoxo complexes. The ligand environment is shown to subtly vary the extent of O–O bond activation in these complexes, and theoretical calculations provide an explanation for these observations. Variable-temperature kinetics studies are also described, which allow us to investigate the mechanism of thermal decay. Strong correlations between experimentally measured and theoretically calculated structural, spectroscopic, and kinetic parameters for these complexes provide compelling evidence for rate-limiting O–O bond cleavage.

Experimental Section

General Methods

All reactions were performed under an inert atmosphere in a glovebox, using standard Schlenk techniques, or using a custom-made solution cell equipped with a threaded glass connector sized to fit an ATR dip probe. Reagents purchased from commercial vendors were

of the highest purity and used without further purification. 3-Methyl-3-mercapto-2-butanone, [Mn^{II} ($S^{Me2}N_4$(QuinoEN))](BPh_4) (1), [Mn($S^{Me2}N_4$(QuinoEN))-(OO^tBu)](BPh_4) (1a), [Mn^{III}($S^{Me2}N_4$(QuinoEN))(OOCm)](BPh_4) (1b), [Mn^{II}($S^{Me2}N_4$(QuinoPN))](PF_6) (2), [Mn^{II}($S^{Me2}N_4$(6-Me-DPPN))](BPh_4) (4), $^tBu^{18}O^{18}OH$, and Et_2PO^tBu were synthesized as previously described.[52–54] [Mn^{II}($S^{Me2}N_4$(6-Me-DPEN))](BPh_4) (3) was synthesized as previously described, using $NaBPh_4$ instead of $NaBF_4$.[54] Acetonitrile (MeCN) and diethyl ether (Et_2O) were rigorously degassed and purified using solvent purification columns housed in a custom stainless steel cabinet, and dispensed via a stainless steel Schlenk line (GlassContour). Methanol (MeOH) and methylene chloride (CH_2Cl_2) were distilled from magnesium methoxide and calcium hydride, respectively, prior to use. IR spectra were recorded on a Perkin-Elmer 1700 FT-IR spectrometer as nujol mulls. ^1H NMR spectra were recorded on a Bruker AV 301 FT-NMR spectrometer and referenced to residual solvent. Magnetic moments (solution state) were obtained using the Evans method as modified for superconducting solenoids.[55] Temperatures were obtained using Van Geet's method.[56] Electronic absorption spectra were recorded using a Varian Cary 50 spectrophotometer equipped with a fiber optic cable connected to a “dip” ATR probe (C-technologies) with a custom-built two-neck solution sample holder equipped with a threaded glass connector. Mass spectra data were recorded on either a Bruker Esquire liquid chromatograph – ion trap mass spectrometer or Hewlett-Packard 5971A gas chromatograph – mass spectrometer. X-ray diffraction data were collected on a Bruker APEX II single crystal X-ray diffractometer with Mo-radiation.

Monitoring the Reaction of 2–4 with ^{t}BuOOH via Electronic Absorption Spectroscopy

In a typical reaction, a 1–2 mM solution of the requisite Mn(II) precursor was prepared in CH_2Cl_2 (3–4 mL) inside a glovebox. The resulting solution was transferred via gastight syringe to a custom-made two-neck vial equipped with a stir bar and septum cap and threaded dip-probe feed-through adaptor that had previously been purged with argon. The solution was then cooled to 258 K using an ethylene glycol/dry ice bath. Tert-butyl hydroperoxide (^{t}BuOOH; 1.5 equiv from a 0.1 M anaerobic stock solution (CH_2Cl_2)) was added via syringe to a stirring Mn(II) solution, along with 2.0 equivalents of triethylamine. Scans were recorded at low temperatures from 300 to 1000 nm in one minute intervals until changes to the absorption spectra ceased for approximately 10 min.

Preparation of FT-IR Samples of [Mn^{III}($S^{Me2}N_4$(QuinoPN))-(OO^tBu)]PF_6)•pentane (2a), [Mn^{III}($S^{Me2}N_4$(6-Me-DPEN))-(OO^tBu)]BPh_4) (3a), [Mn^{III}($S^{Me2}N_4$(6-Me-DPPN))(OO^tBu]-(BPh_4)·Et_2O (4a)

Solid material of 2a–4a was obtained from *in situ* reaction mixtures via low-temperature precipitation. In a typical experiment, a 20–35 mM supersaturated solution of the appropriate Mn(II) precursor was prepared in MeCN (2–3 mL) in a glovebox The resulting solution was then transferred to an anaerobic vial, cooled to −40 °C using a ethylene glycol/dry ice bath, followed by the addition of 2.0 equiv of ^{t}BuOOH from an anaerobic 1 M stock solution (CH_2Cl_2). The resulting reaction mixture was allowed to stir for 5–7 min at −40 °C. Pre-cooled Et_2O (10–15 mL) was then quickly added to the reaction mixture to promote the rapid precipitation of solid material. The resulting solid was isolated via filtration through a cold frit, mixed with cold Nujol, and immediately analyzed by FT-IR The identity of the sample was verified by redissolving the solid material in cold CH_2Cl_2, and recording the UV/vis spectra, which revealed spectral features identical to those observed in an in situ low-temperature generated sample.

Determination of the Solution Magnetic Moment of ^{t}Butyl-Peroxos 2a−4a

Crystalline samples of 2a−4a were obtained by layering cold pentane (or Et_2O) onto a concentrated in situ CH_2Cl_2 reaction mixture generated at −40 °C and cooled to −80 °C.

Following diffusion of the pentane (or Et_2O) into the CH_2Cl_2 the resulting crystals were filtered through a cold frit, washed with pre-cooled Et_2O, weighed on an analytical balance in an NMR tube, and then transported down to the NMR room. Once in the NMR room, a known volume of pre-cooled (in a bed of dry ice) CD_2Cl_2 containing TMS, was then added to the crystalline samples immediately prior data collection. Magnetic moments obtained in this manner, (μ_{eff} = 4.78 BM (2a), 4.79 BM (3a), 4.89 BM (3b)) were close to the spin-only value (4.90 BM) for high-spin (S=2) Mn(III), indicating that very little, if any, decomposition had occurred over the course of the data collection.

Ab Initio Density Functional Theory (DFT) Calculations

All calculations were performed using the ORCA program package.[57] Geometries were optimized based on the crystal structures, and a high-spin state, using the TPSS functional and the def2-TZVP(-f) basis set in combination with the def2-TZV/J auxiliary basis sets for the Coulombic density fitting approximation.[58–65] Scalar relativistic effects were accounted for using the ZORA approximation and a conductor like screening model was applied using dichloromethane as the solvent of choice (COSMO, CH_2Cl_2 ε = 9.08). Mnimum deviations from the crystallographically determined geometries, bond angles and bond distances were obtained when intramolecular van der Waals interactions were accounted for using the vdw10 keyword. All calculations were performed using an integration grid of 5 (Grid5) for the complex and a grid of 7 for the Mn(III) metal center. Relaxed surface scans were performed on the O–O bond length from 1.1 to 1.6 Å to explore the impact of the alkylperoxo bond length on the metal ion's coordination sphere.

X-ray Crystal Structures of ^{t}Butyl Peroxos 1a-4a, and Cumenyl Peroxo 3b

A blue prism of 2a immersed in oil with dimensions 0.15 × 0.15 × 0.05 mm^3 was mounted on a glass capillary. Data were collected at –173 °C. The crystal-to-detector distance was 40 mm, and the exposure time was 10 s per degree for all sets. The scan width was 0.5°. Data collection was 100% complete to 25° in ϑ. A total of 49,617 merged reflections were collected covering the indices h = –12 to 12, k = –17 to 17, and l = –28 to 28; 6557 reflections were symmetry independent, and the R_{int} = 0.0875, indicating the data was slightly less than average. Indexing and unit cell refinement indicated a monoclinic P lattice, and the space group was found to be $P2_1/n$ (No. l4).

A faint blue prism of 3a immersed in oil with dimensions 0.15 × 0.10 × 0.05 mm^3 was mounted on a glass capillary. Data were collected at −173 °C. The crystal-to-detector distance was 40 mm and the exposure time was 120 s per degree for all sets. The scan width was 0.5°. Data collection was 98.9% complete to 25° in ϑ. A total of 76,962 merged reflections were collected covering the indices h = −20 to 20, k = −30 to 30, and l = −13 to 13; 4716 reflections were symmetry independent, and the R_{int} = 0.4200, indicating the data were problematic. Indexing and unit cell refinement indicated a primitive orthorhombic lattice, and the space group was found to be $Pna2_1$ (No. 33).

A blue plate of **3b** immersed in oil with dimensions 0.10 × 0.05 × 0.05 mm^3 was mounted on a glass capillary. Data were collected at −173 °C. The crystal-to-detector distance was 40 mm, and the exposure time was 20 s per degree for all sets. The scan width was 0.5°. Data collection was 98.8% complete to 25° in ϑ. CLL_NOW[54] was used to perform a 4.3° rotation twin operation about (0 0 1) to prevent considerable overlap of diffraction peak intensities from different domains of the sample. Multidomain integration with SAINT within the APEX2 software package and an absorption correction with TWINABS[55] removed the overlap. A total of 66,667 merged reflections were collected covering the indices h = −15 to 15, k = −16 to 11, and l = 0 to 18; 9356 reflections were symmetry independent, and the R_{int} = 0.1265, indicating the twin-refined data were acceptable.

Indexing and unit cell refinement indicated a triclinic lattice, and the space group was found to be $P\bar{1}$ (No. 2). Molecules of CH_2Cl_2 and Et_2O were found to occupy the same space with a 2:1 ratio.

A purple prism of **4a** immersed in oil with dimensions 0.25 × 0.20 × 0.10 mm^3 was mounted on a glass capillary. Data were collected at −173 °C. The crystal-to-detector distance was 40 mm, and the exposure time was 10 s per degree for all sets. The scan width was 0.5°. Data collection was 98% complete to 25° in θ. A total of 32,237 merged reflections were collected covering the indices h = −11 to 11, k = −14 to 17, and l = −19 to 19; 7856 reflections were symmetry independent, and the R_{int} = 0.0766, indicating the data were of average quality. Indexing and unit cell refinement indicated a monoclinic P lattice, and the space group was found to be $P\bar{1}$ (No. 2).

All data were integrated and scaled using SAINT, SADABS within the APEX2 software package by Bruker. Solutions by direct methods (SHELXS, SIR97) produced a complete heavy atom phasing model consistent with the proposed structure. The structure was completed by difference Fourier synthesis with SHELXL97. Scattering factors were obtained from Waasmair and Kirfel.[66] Hydrogen atoms were placed in geometrically idealized positions and constrained to ride on their parent atoms with C–H distances in the range 0.95–1.00 Å. Isotropic thermal parameters (U_{eq}) for the hydrogens were fixed such that they were 1.2U_{eq} of their parent atom U_{eq} for CH's and 1.5U_{eq} of their parent atom U_{eq} in case of methyl groups. All non-hydrogen atoms were refined anisotropically by full-matrix least-squares. Crystal data for **2a, 3a, 3b,** and **4a** are provided in Table 1, and selected metrical parameters are provided in Table 3.

Variable-Temperature Kinetics and Reactivity of Alkyl Peroxos 1a, 2a, 3a, 3b, and 4a

In a typical experiment, 4 mL (CH_2Cl_2) of a 1–2 mM solution of a Mn(II) complex was prepared under an inert atmosphere in a glovebox. The resulting solution was then transferred via gastight syringe to a custom-made two-neck vial equipped with a stir bar and septum cap and a threaded dip-probe feed-through adaptor that had previously been purged with argon. The solution was brought to the desired temperature using a low-temperature bath (258 K (ethylene glycol/dry ice), 268 K (NaCl/ice water), 273 K (ice water)). Gentle stirring was maintained throughout the course of each experiment to maintain solution homogeneity. An immediate production of the corresponding Mn(III)–alkylperoxo intermediate as indicated by its UV/vis absorption spectrum was caused by the addition of 1.5 equiv of ^{t}BuOOH in a single addition to the Mn(II) solution. Decay of the respective intermediate was monitored at 592 nm (**1a**), 580 nm (**2a**), 594 nm (**3a**), 590 nm (**3b**), or 450 nm (**4a**) once formation of the corresponding Mn(III)–OOR complex was complete. UV/vis scans were recorded at 1 min intervals until no further change in absorbance intensity occurred for at least 10 min. First-order rate constants were calculated by plotting $\ln[(A_x - A_\infty)/(A_0 - A_\infty)]$ vs time. Experiments were conducted in at least triplicate under any given set of conditions.

Reactions between the Mn(III)–OOR complexes and various substrates were performed in an analogous fashion by adding the substrate to the fully formed intermediate in a single aliquot at either 273 or 298 K. Concentrated stock solutions of each substrate were prepared under an inert atmosphere in a glovebox and transferred to the reaction solution with a gastight syringe. After changes in absorbance values ceased for at least 10 min, insolubles were removed from the crude reaction mixtures by filtration through a fine-fritted filter. Soluble organics were diluted with an appropriate amount of CH_2Cl_2 and analyzed by GC/MS. Products were identified by comparison with authentic standards and product yields were determined using calibration curves referenced to 1,4-dioxane as an internal standard.

General Workup Procedure for Analysis of the Thermal Decomposition Products From $[Mn^{III}(S^{Me2}N_4(QuinoEN))\text{-}(OO^tBu)](BPh_4)$ (1a), $[Mn^{III}(S^{Me2}N_4(QuinoPN))(OO^tBu)]\text{-}(PF_6)\cdot$pentane (2a), $[Mn^{III}(S^{Me2}N_4(6\text{-Me-DPEN}))(OO^tBu)](BPh_4)$ (3a), $[Mn^{III}(S^{Me2}N_4(6\text{-Me-DPEN}))(OOCm)](BPh_4)$ (3b), and $[Mn^{III}(S^{Me2}N_4(6\text{-Me-DPPN}))(OO^tBu](BPh_4)\cdot Et_2O$ (4a)

In a typical reaction, a 1–2 mM solution of the desired intermediate was prepared in a fashion identical to that described above at 273 K in CH_2Cl_2. Reactions were allowed to progress until the absorption features of the respective Mn(III)–OOR intermediate bleached and no further changes to the absorption spectrum were observed for at least 1 h. The final reaction mixtures were observed to contain white insoluble solids, black insoluble solids, in addition to CH_2Cl_2 soluble components. Insolubles were removed by filtering each reaction through a fine-fritted filter. In order to indentify the CH_2Cl_2 soluble reaction mixture components, all volatiles were distilled *in vacuo* to a separate container. Nonvolatile components remaining in the initial sample container were then analyzed by ^{1}H NMR and ESI-MS, while volatile components were analyzed by ^{1}H NMR and GC/MS. The clear and black insoluble reaction mixture components were separated by suspending these products in $CHCl_3$, which caused the white product to dissolve, leaving behind the insoluble black precipitate. After filtration to separate the black insoluble precipitate, the resulting $CHCl_3$ solution was dried *in vacuo*, redissolved in fresh $CDCl_3$, and analyzed by ^{1}H NMR, ESI-MS, and/or GC/MS.

Results and Discussion

Coordinatively unsaturated, reduced $[Mn^{II}(S^{Me2}N_4(QuinoEN))]^+$ (**1**) was shown previously to react with *tert*-butyl hydroperoxide (^{t}BuOOH) and cumene hydroperoxide (CmOOH) to form the corresponding oxidized high-spin ($S = 2$) Mn(III) – alkylperoxo complexes $[Mn^{III}(S^{Me2}N_4(QuinoEN))(OO^tBu)]^+$ (**1a**) and $[Mn^{III}(S^{Me2}N_4(QuinoEN))(OOCm)]^+$(**1b**), respectively (Scheme 1).[32] Although metastable, both **1a** and **1b** proved stable enough to permit crystallographic characterization, thereby providing the first examples of end-on Mn(III)(η^1-peroxo) complexes. Five-coordinate **1** was also recently shown to react with dioxygen to afford a rare example of a structurally characterized mono-oxo bridged dimer, $[Mn^{III}(S^{Me2}N_4(QuinoEN)]_2\text{-}(\mu\text{-O})(PF_6)_2\cdot Et_2O$.[54] Three additional coordinatively unsaturated Mn(II) complexes (Scheme 2), $[Mn^{II}(S^{Me2}N_4(2\text{-QuinoPN}))](PF_6)$ (**2**), $[Mn^{II}(S^{Me2}N_4(6\text{-Me-DPEN}))](BF_4)$ (**3**), and $[Mn^{II}(S^{Me2}N_4(6\text{-Me-DPPN}))]\text{-}(BPh_4)$ (**4**), were included in this report,[54] each of which was shown to react with O_2 to afford an unsupported oxo-bridged dimer. Given the similar structural and reactivity properties of **1–4**, we decided to explore the reactivity of **2–4** with alkyl hydroperoxides in order to provide a more structurally diverse library of end-on Mn(III)(η^1-peroxo) compounds.

Reaction Between *tert*-Butyl Hydroperoxide and $[Mn^{II}(S^{Me2}N_4(QuinoPN))]^+$ (2), $[Mn^{II}(S^{Me2}N_4(6\text{-Me-DPEN}))]^+$ (3), and $[Mn^{II}(S^{Me2}N_4(6\text{-Me-DPPN}))]^+$ (4)

Dichloro methane solutions of five-coordinate **2–4** (Scheme 2) change from colorless to blue upon the anaerobic addition of ^{t}BuOOH. At ambient temperature, these blue solutions persist for only ~10–30 min before they turn pale yellow (*vide infra*), indicating that the species formed are metastable. As was noted previously for **1a** and **1b** (Scheme 1), base (Et_3N) was found to increase the stability of these metastable species; in the absence of base the blue color fades more rapidly. When these reactions are monitored via electronic absorption spectroscopy at low temperatures (258 K), two distinct absorption bands grow in between 350 and 420 nm and 560–605 nm (Table 2). The relative energies and intensities of these absorption bands (Figures S-1–S-4 in Supporting Information [SI]) are comparable to those previously reported for alkylperoxo-ligated **1a**,[32] suggesting that the species formed, **2a–4a**, are also alkylperoxos. Solid samples of **2a–4a** for the measurement of extinction coefficients and IR spectra were obtained via the addition of cold Et_2O (10–15 mL) to a

low-temperature (−40 °C), *in situ* generated reaction mixture, followed by filtration through a cold frit immediately (2−3 min) prior to data collection. Compounds **2a–4a** are slightly more stable in the solid state, but still require the low-temperature generation of freshly prepared samples immediately prior to each experiment. Titration experiments show that 1.5−1.8 equiv of ^{t}BuOOH are required to fully maximize (Figures S-5, S-6 in SI) the electronic absorption features of **2a–4a** as is illustrated in Figure 1 for compound **4**.

Evidence to support the formulation of blue metastable **2a– 4a** as Mn(III)−OO^{t}Bu alkylperoxo species was obtained via mass spectrometry, FT-IR, and solution magnetic moment measurements. Electrospray ionization mass spec (ESI-MS) experiments were performed using aliquots of low temperature *in situ* generated reaction mixtures (**1–4** + 1.8 equiv of ^{t}Bu^{16}O^{16}OH). Prominent peaks are observed in the ESI-MS at *m*/*z* = 598.8 (**2a**, *m*/*z* = 598.6 (calc)), 513.0 (**3a**, *m*/*z* = 513.6 (calc)), and 526.9 (**4a**, *m*/*z* = 526.6 (calc)), respectively (Figures S-7−S-12 in SI). Upon preparation with ^{t}Bu^{18}O^{18}OH, each of these peaks increases by approximately 4 mass units to *m*/*z* = 602.7 (**2a**), 516.9 (**3a**), and 530.8 (**4a**), confirming the presence of two ^{18}O atoms in each complex (Figures S-7−S-12 in SI). The presence of a ^{t}BuOO^{-} ligand in 2a–4a is also supported by vibrational data (FT-IR) for both the ^{16}O- and ^{18}O- isotopic derivatives. In order to ensure that the counterion did not dominate the IR spectra in the region of interest (900– 700 cm^{-1}), the BPh_4^- salt of each complex was prepared. As illustrated in Figure 2 for compound **3a**, isotopically sensitive stretches (Table 2) are observed in the range expected for a peroxo.[47,68–75] Each of these stretches (Figures S-13, S-14 in SI, Figure 2) falls in the reported range (885–896 cm^{-1}) for the handful of vibrationally characterized Mn(III)–peroxos,[15,42,43] including alkylperoxo **1a** (888 cm^{-1}).[32] The isotopic shifts (Δ^{18}O^{18}OR) vary by as much as 14–20 cm^{-1} from that predicted (44 cm^{-1}) based upon a harmonic oscillator model, indicating that the observed vibrational modes involve more than a simple diatomic O–O stretch.[46,49] Samples for solution magnetic moment determination (i.e., the Evan's method[55]) were freshly prepared immediately (~2 min) prior to data collection by filtering low-temperature (−80 °C) grown crystals through a cold frit, washing with precooled Et_2O, quickly weighing them on an analytical balance in an NMR tube, and then adding precooled (−78 °C) CH_2Cl_2 immediately prior to the insertion of the sample into the spectrometer. Solution magnetic moments were estimated on the basis of a molecular weight that included the manganese cation, anion, and no solvents of crystallization. The resulting moments (μ_{eff} = 4.78 μ_B (**2a**); 4.79 μ_B (**3a**); 4.89 μ_B(**4a**)) were close to the spin-only value (4.90 μ_B) for high-spin (S = 2) Mn(III), indicating that the samples were reasonably pure and that the manganese ions were in the +3 oxidation state.

Structural Characterization of Metastable [Mn^{III}(S^{Me2}N$_4$(QuinoPN))(OO^{t}Bu)](PF$_6$)·pentane (2a), [Mn^{III}(S^{Me2}N$_4$(6-Me-DPEN))(OO^{t}Bu)](BPh$_4$) (3a), [Mn^{III}(S^{Me2}N$_4$(6-Me-DPPN))(OO^{t}Bu](BPh$_4$)·Et$_2$O (4a)

Evidence to definitively support the description of metastable **2a–4a** as Mn(III)–OOR compounds was obtained via X-ray crystallography. X-ray-quality single crystals were obtained by layering either pentane or Et_2O onto concentrated CH_2Cl_2 solutions of **2a–4a** at −80 °C. ORTEP diagrams for **2a–4a** are shown in Figure 3, and selected metrical parameters are provided in Table 3. Although the metrical parameters for **1a** have been reported elsewhere,[32] they are also included in Table 3 for comparison. Each akylperoxo-bound complex, **2a–4a**, is monocationic as is indicated by the presence of a single anionic counterion (PF_6^- for **2a**, and BPh_4^- for **3a** and **4a**) per Mn complex. The Mn(III) oxidation state in each complex is clearly evident from the Mn(III)–S(1) bond distances (Table 3), which are ~0.1 Å shorter than those of the corresponding reduced Mn(II) complexes, **1–4**,[54] and close to that of alkylperoxo-bound **1a**.[32] Each Mn(III) ion contains an akylperoxo ligand coordinated through its terminal oxygen O(1) *trans* to an imine nitrogen N(1), and *cis* to

both a thiolate sulfur S(1) and tertiary amine N(2). Two N-heterocyclic amine nitrogens, N(3) and N(4) (quinolines for **2a**, 6-Me-pyridines for **3a** and **4a**), lie *trans* to one another at a distance from the Mn(III) ion (2.349(7)–2.522(8) Å; Table 2), which is significantly greater than the sum of their ionic and covalent radii (2.105 Å).[67] The geometry of complexes **1a–4a** is therefore close to being four-coordinate square planar. Elongation of the two *trans* Mn···N(3) and Mn···N(4) interactions is most likely driven by the stabilization of an odd electron in the "e_g*" set of d-orbitals (akin to Jahn–Teller distortion) and provides additional evidence that the Mn(III) ions are high-spin d^4. Computational studies (*vide infra*) show, however, that the elongated Mn···N(3) and Mn···N(4) distances also provide relief from steric interactions between hydrogens located on the N-heterocyclic amines and the gem-dimethyls adjacent to the sulfur. Sterics do not directly influence the ^{t}BuOO^{-} ligand, however (*vide infra*), which is spatially quite separated from both the gem-dimethyls and 6-Me-pyridine substituents. The Mn(III)···N(3,4) separation represents the largest structural variable (±0.17 Å) within this particular series; the Mn(III)–O(1), M(III)–N(1), Mn(III)–N(2), and Mn(III)–S(1) distances are well within acceptable bonding ranges, and display little variation (±0.02 Å, ± 0.03 Å, ± 0.04 Å, and ±0.03 Å, respectively). As was observed with the five-coordinate Mn(II) precursors **1**–**4**,[54] the insertion of an extra methylene unit into the ligand backbone is found to much more noticeably influence the structures than does the identity of the N-heterocyclic amine (6-Me-pyridine vs quinoline). In propyl-linked **2a** and **4a** (Figure 3), the extra methylene linker introduces flexibility that allows the metal ion to attain a more idealized pseudo-octahedral geometry with angles closer to 180° and 90°, respectively (Table 3). This results in better orbital overlap with the alkylperoxo ligand (*vide infra*).

Metrical parameters associated with the ^{t}BuOO^{-} ligands in **2a–4a** (Table 3) are all within the anticipated ranges for metal–alkylperoxo species,[68–72] roughly correlate with vibrational parameters (Table 4) and are consistent with an end-on coordination mode. The peroxo Mn(III)–O(1) bond lengths in **2a–4a** (range: 1.840(4)–1.853(6) Å) are slightly shorter than that of **1a** (1.861(5) Å), and fall at the short end of the limited number of reported Mn(III)–peroxos (range: 1.85– 1.90 Å),[34,38,41–43] all of which happen to contain a side-on η^2-bound peroxo. Compared to reduced [Tp ^{tBu,tPr} Mn(II)-(OO^{t}Bu)] (1.964 Å),[72] the peroxo Mn–O(1) bonds in **2a– 4a** are especially short. The former would have an additional antibonding e_g* electron which would contribute to a lengthening of the Mn(II)–O bond. The lower coordination number, and resulting increase in metal ion Lewis acidity, would also contribute to the shorter Mn–O(1) bonds in **1a– 4a**. The relatively obtuse Mn(III)–O(1)–O(2) angles, and short Mn–O(1) bond distances would be consistent with at least some Mn=OOtBu double bond character.[46,49] The O(1)–O(2) peroxo bond lengths in **1a–4a** span the range 1.431(5)–1.468(7) Å, which in the case of Et-linked **1a** and **3a** (1.457(7) and 1.468(7) Å, respectively) is significantly longer than all structurally characterized examples of mononuclear Mn(III)–peroxos (range O–O = 1.403(4)–1.428(7) Å), [(TPP)Mn(O_2)](K(K222)),[41] [Mn(14-TMC)(O_2)]$^{+}$,[38] [Mn-(13-TMC)(O_2)]$^{+}$,[34] Mn(O_2)(3,5-^{i}Pr$_2$pzH)(HB(3,5-^{i}Prpz)$_3$),[42] and Tp^{iPr2} Mn(η^2-O_2) (im^{Me}H),[43] all of which contain a side-on η^2-peroxo. An end-on binding mode of the tBuOO^{-} ligand in **2a–4a** is confirmed by the long distance separating the Mn(III) ion from the distal oxygen (Mn···O(2) = 2.861 Å, 2.769 Å, and 2.901 Å), which is nearly a full 1 Å longer than that of the side-on Mn(III)(η^2-O_2) complexes mentioned above.[38,41–43] The less acute Mn–O(1)–O(2) angles of **2a–4a** (121.1(3)°, 112.44(4)°, and 124.25(3)°, respectively) are also consistent with an end-on binding mode. These angles are similar to, albeit larger than, that of **1a** (109.14°), but nearly twice as large as those (66°–70°) found in the side-on Mn(III)(η^2–O_2) complexes mentioned above.[34,38,41–43]

Correlation Between Structural and Spectroscopic Parameters

Changes to the ligand backbone of the series of N-heterocyclic amine Mn–alkylperoxo compounds described herein causes subtle variations in the metal–ligand bond distances and angles, and systematic changes to the electronic structure. The long Mn···N(3) and Mn···N(4) distances increase the metal ion Lewis acidity (*vide infra*) resulting in shorter metal ligand bonds (Table 3). As shown in Table 4, the average Mn···N(3,4) distance in complexes **1a–4a** decreases as a methylene unit is removed from the ligand backbone. Although exceedingly long, these nitrogens (N(3) and N(4)) are found to perturb the Mn ion enough to influence its properties. For example, the highest energy electronic absorption band (Figures S-1–S-4 in SI) systematically blue-shifts as the average Mn···N(3,4) distance decreases (Table 4, Figure S-16 in SI). The N-heterocyclic amines also influence the alkyl peroxo's metrical parameters. As N(3) and N(4) move in closer to the metal ion, the Mn–O(1) and O(1)– O(2) distances increase and the peroxo becomes more activated (Figure 4 and Figure S-17 in SI). This observed trend[78] can be explained by empirical and computational studies which show that electron-donating ligands promote longer, more activated peroxo O–O bonds.[33–35,71,73–77] As the Mn····N(3,4) separation decreases in **1a–4a** electron density increases at the Mn ion. As shown in Figure 4, the inverse correlation between the Mn····N(3,4) and O(1)–O(2) distances in **1a–4a** is strong (R^2 = 0.99). There is very little correlation between the Mn–S(1) and O(1)–O(2) distances (Figure S-22 in SI). We also see a strong correlation between the energy of λ_{max} and the alkylperoxo O(1)–O(2) bond length (Figure 5, Table 4) of **1a–4a**. The strong correlation between these parameters provides evidence to support the crystallographically determined differences in O–O bond lengths, and provides clues regarding the assignment of this electronic absorption feature. Although the O–O bond distances for Et-linked **1a** and **3a** are indistinguishable from one another (Figure 5) based on the crystallographic error (esds in Table 3), these distances are distinctly different from those of Pr-linked **2a** and **4a**.

The observed systematic blue shift in λ_{max} upon elongation of the peroxo O–O bond in **1a–4a** agrees with TD-DFT-predicted trends for the π_v*(O–O) → Mn charge transfer band of peroxo-ligated $[Mn^{III}(O_2)(L^7py_2^{Me})]^+$,[35] and the theoretically calculated energy (λ_{max} = 442 nm) approximately matches our experimentally measured transition energy (Table 4). On this basis, we have tentatively assigned the highest energy band associated with **1a–4a** as a π_v*(O–O) → Mn charge transfer band (Figures S-1–S-4 in SI). The extinction coefficients for these transitions display a roughly linear relationship with the Mn(III)–O(1)–O(2)-R dihedral angles (139.5° (**1a**), 131.8° (**2a**), 163.6° (**3a**), 126.6° (**4a**)), with larger dihedral angles resulting in higher extinction coefficients (Figure S-19 in SI). This relationship can be explained by the fact that extinction coefficients are expected to increase as orbital overlap (between the π_v*(O–O) orbital and the symmetry-appropriate Mn d-orbital, *vide infra*) increases, with maximum overlap at a dihedral angle of 180°.[79] There are no direct correlations between the lower-energy visible absorption features of **1a–4a** (λ_{max} = 560–605 nm; Figures S-1–S-4 in SI) and any metrical parameter that would permit a tentative spectral assignment; however, the relatively low extinction coefficients for these bands would be at least consistent with ligand field transitions.

In addition to the observed shifts to the π_v*(O–O) → Mn charge transfer bands, the ν(O–O) vibrational energies also shift to higher energies as the O(1)–O(2) bond lengths in **1a– 4a** decrease (Table 4). However the correlation coefficient (0.81) for ν(O–O) vs O(1)–O(2) distance (Figure S-16 in SI) is modest, suggesting that the force constants differ from complex to complex, possibly due to a change in hybridization of O(1). A change in O(1) hybridization (from sp^3 to sp^2) is indicated by the systematic change in Mn(III)–O(1)–O(2) bond angles (from 109.2(4)° to 124.2(3)°; Figures S-20 and S-21 in SI). There is also a wide range of Mn(III)–O(1)– O(2)– ^{t}Bu dihedral angles (139.5° (**1a**), 131.8° (**2a**), 163.3° (**3a**),

126.6° (**4a**)) suggesting that varying degrees of coupling to the ^{t}Bu-group might perturb the vibrational modes.[46,69] The strong correlation between crystallographically determined alkylperoxo O–O bond distances and spectroscopic parameters for **1a–4a** (Table 4, Figure 5) provides experimental evidence supporting the accuracy of the observed crystallographic differences in O–O bond length. Computational studies support this

Ab Initio Density Functional Theory (DFT) Calculations

Geometry optimizations for 1a–4a were carried out using *ab initio* density functional theory (DFT), and potential correlations between peroxo O–O bond length and N-heterocyclic amine Mn···N(3,4) distances were examined (for **3a** and **4a**) using relaxed surface scans. Initial geometry optimizations showed deviations in Mn···N(3,4) separations (±0.05 Å), and Mn–O–O angles (up to 10°), relative to the crystallographic structures (Table S-1 in SI). However, the inclusion of van der Waals corrections greatly improved the agreement between calculated and experimental parameters (±0.03 Å difference in Mn···N(3,4) separation, and less than ~3° difference in Mn–O–O angle), indicating that steric interactions are likely responsible for the long Mn···N(3,4) distances and coordinative unsaturation in **1a–4a**. The calculated peroxo O–O bond lengths (Table S-1 in SI) were found to be indistinguishable for the two N-heterocyclic amines (6-Me-pyridine vs quinoine), but fall into two distinct groups, depending on the ligand backbone (Pr- vs Et-linker). As is observed experimentally, Et-linked **1a** and **3a** are predicted to have shorter Mn···N(3,4) distances and longer O–O bonds (by ~0.01 Å) relative to those of Pr-linked 2a and 4a (Table S-1 in SI). However, the theoretically calculated difference is not as large as that seen in the crystal structures. To further understand the differences between structures containing an Et- vs Pr-backbone, Mulliken charge densities were considered. The Mn center of Et-linked **3a**, which has the longest O–O bond in the series (1.468(7) Å; Table 2), was theoretically determined to have the lowest Mulliken charge density (+0.42), and hence the lowest Lewis acidity (Table S-2 in SI). Whereas, the Mn center of Pr-linked 4a, which has the shortest crystallographically determined O–O bond in the series (1.431(5) Å), was theoretically determined to have the highest Mulliken charge density (+0.50) and, hence, the highest Lewis acidity (Table S-2 in SI).

In order to understand the relationship between the O–O bond length and the metal ion coordination sphere, relaxed surface scans were performed. For this study, the O–O bond length was varied from 1.1 to 1.6 Å, while optimizing all other coordinates for Et-linked **3a** vs Pr-linked **4a**, (Table S-3 in SI). As the O–O bond was increased in length, charge density became more localized on the proximal peroxo oxygen (varying from −0.22 (O–O = 1.1 Å) to −0.40 (O–O = 1.6 Å). The changes in charge density at the Mn ion were found to be relatively small. This may be attributed to the fact that the entire ligand framework is involved in modulation of the charge distribution. As the calculated apical Mn-N bond length increases (from ~2.03 Å (**1a**/**3a**) to ~2.11 Å (**2a**/**4a**)), more charge density is predicted to be localized on the apical nitrogen, and less on the thiolate sulfur. This would suggest that sulfur acts as a charge donor that compensates[80] for electron density fluctuations at the metal center.

The bonding molecular orbitals of $[Mn^{III}(S^{Me2}N_4(6\text{-Me-DPPN}))(OOtBu)]^+$ (**4a**) illustrate why an increased localization of charge on the peroxo would lengthen the O–O bond. The Mn ion contribution to the Mn– O(1) π-bonding MO of Figure 6 decreases (from ~33% to ~27%) as the O–O bond gets longer (from 1.2 Å to 1.5 Å), whereas the peroxo contribution increases from ~9.4% to 10.3%.[81] The lengthening of the O–O bond is thus a consequence of an increased localization of charge density in a π(Mn–O) orbital (shown in Figure 6) that is antibonding with respect to the peroxo O–O bond. These theoretical results are supported by literature precedent[33–35,71,73–76] and agree with the bonding picture, established for

Fe(III)–OOR compounds, which also includes a π(Fe–O) bond formed via overlap between a π_v*(O–O) orbital and a symmetry-appropriate metal d orbital.[46,49] In both cases, the end-on η^1-peroxo behaves as a π-donor ligand. With Lewis acidic metal ions, π-donation from the filled peroxo π_v*(O–O) orbital results in a stronger O–O bond. Longer peroxo O–O bonds are observed with more electron-rich metal centers not only with the members of the series, **1a** and **3a**, containing shorter Mn···N^{py,quin} interactions, but also with Cu(II), Co(III), Fe(III), and other Mn(III) com-plexes. [33–35,71,73–76,78]

Variable-Temperature Decay Kinetics for Alkylperoxo Compounds 1a–4a

Temperature-dependent kinetic studies were performed in order to provide additional experimental evidence supporting the structural and spectroscopic trends described above. As described below, we observe strong correlations between structural and kinetic parameters consistent with a decay mechanism involving rate-limiting O-O bond cleavage. Each metastable Mn(III)–OOR complex **1a–4a** was found to decay in solution over a relatively short period of time, even at low temperatures. The details regarding the mechanism of this decay reaction were obtained using variable-temperature kinetics probed by electronic absorption spectroscopy in CH_2Cl_2. Previously, we showed that **1a** undergoes a first-order thermal decomposition process at 258 K in CH_2Cl_2 with a rate constant that is insensitive to the presence of electrophilic and nucleophilic organic substrates, as well as dioxygen.[32] Herein we examine the reaction kinetics for the other members of the series **2a-4a**, in addition to the temperature-dependent kinetics for all of the compounds described herein including **1a**. Time-dependent changes in absorption (at 592 nm (**1a**), 580 nm (**2a**), 594 nm (**3a**), or 450 nm (**4a**)) were measured at several temperatures between 258 and 293 K, over at least three half-lives. Linear fits to $\ln[(A_t - A_\infty)/(A_i - A_\infty)]$ vs time plots indicated that the reaction was first-order in Mn−alkylperoxo complex at all of the temperatures examined. Correlation coefficients were significantly lower (R^2 = 0.4−0.7) for second-order ($[(A_i - A_\infty)/(A_t - A_\infty)]$ vs time) plots. First-order rate constants were obtained as described in the Experimental Section and are assembled in Table 5. A representative time-dependent absorption vs wavelength stack plot (Figure S-23 in SI), and the corresponding first order kinetics plot, are shown in Figure 7. Half-lives were found to be independent of the initial peroxo intermediate concentration (1−2 mM), providing additional support for a first-order reaction. Activation parameters (Table 5) for the thermal decay of each Mn(III)−OOR complex (Figure S-23 in SI) were obtained from linear fits to Eyring plots ($\ln(k/T)$ vs T^{-1}; Figure 8, and Figures S-24–S-26 in SI). Initial inspection of the data (Table 5) shows that both $\Delta H^{\ddagger}$ and $\Delta S^{\ddagger}$ each fall within a relatively narrow range of one another, consistent with the thermal decay of **1a–4a** proceeding via a similar mechanism. If we include a cumenyl peroxo derivative of **3a**, [Mn^{III}(S^{Me2}N$_4$(6-Me-DPEN))-(OOCm](BPh$_4$) (**3b**), in this study, then we see very similar activation parameters (Table 5) suggesting that the R-group (of Mn(III)–OOR) does not dramatically influence the decay mechanism. In order to confirm that **3b** was indeed a peroxo and to determine whether the R group influences the structure, single crystals were grown for crystallographic characterization of metastable **3b**. As shown by the ORTEP diagram of [Mn^{III}(S^{Me2}N$_4$(6-Me-DPEN))(OOCm](BPh$_4$) (**3b**) in Figure 9, the metrical parameters of Table 3, electronic absorption spectrum of Figure S-27 in SI, and Eyring plot of Figure S-28 in SI, it is clear that the R group has very little influence on the structural and spectroscopic properties. An enthalpy–entropy compensation effect[82] is also apparent from a plot of $\Delta H^{\ddagger}$ vs $\Delta S^{\ddagger}$ for all five compounds **1a–4a** and **3b** (Figure S-29 in SI), providing additional evidence for a common decay mechanism (although we recognize that the validity of this particular relationship is debated and has been scrutinized).[83] Strong correlations between the activation parameters ($\Delta H^{\ddagger}$ and $\Delta S^{\ddagger}$) and the crystallographically determined alkylperoxo O(1)–O(2) bond lengths for **1a–4a** and **3b** provide the most significant clues regarding a likely mechanism for the observed thermal decay process. As shown in Figure 10, the

activation parameters $\Delta H^{\ddagger}$ and $\Delta S^{\ddagger}$ progressively decrease as the O(1)– O(2) bond length increases. Additionally, the half-life ($\tau_{1/2}$= 56.4 min) of the peroxo complex (Et-linked **3a**) with the longest O–O bond (1.468(7) Å) is significantly shorter than that ($\tau_{1/2}$ = 110 min) of the peroxo complex (Pr-linked 4a) with the shortest O–O bond (1.431(5) Å). This provides additional evidence that the crystallographically determined bond lengths are accurate and the error is overestimated. The decay occurs much more slowly for compounds (**2a**, **4a**) containing an extra methylene unit and longer Mn···$N(3,4)_{avg}$ separation (Table 5), showing that the ligand backbone and N-heterocyclic amines indeed influence reactivity. There is very little correlation between the activation parameters $\Delta H^{\ddagger}$ (or $\Delta S^{\ddagger}$) and the Mn(III)-O(1) bond lengths, on the other hand (Figures S-31, S-32 in SI). All of this d*ata would be consistent with a mechanism involving rate-determining cleavage of the O–O, as opposed to Mn–O bond.*.[82,84,85] The activation enthalpy $\Delta H^{\ddagger}$ decreases as ν_{O-O} decreases (Figure S-30 in SI), which is also consistent with this mechanism. One would expect that a rate-determining reaction step involving O–O bond cleavage would display a positive activation entropy, which is contrary to our experimental results. Negative activation entropies are also seen in O–O bond-cleaving reactions involving high-spin (S = 5/2) Fe(III)–OO^{t}Bu complexes,[86] and peroxo-bridged (TMP)Fe-(III)–O–O–Fe(III)(TMP).[87] One possible explanation for the negative activation entropies seen with the peroxo compounds described in this study is that the transition state leading to successful cleavage of the O–O bond has a shorter, more ordered interaction between the Mn ion and N(3,4). This would make sense given that longer O–O bonds were found to result from shorter Mn(III)–$N(3,4)_{avg}$ distances. It is also possible that solvent effects are responsible.

Thermal Decomposition Products from 1a–4a and 3b, Both in the Presence and Absence of Organic Substrates

The products formed following thermal decay of **1a–4** and **3b** were analyzed via ^{1}H NMR, GC/MS, and ESI-MS. For each complex, final reaction mixtures were found to contain white and black solids, in addition to CH_2Cl_2-soluble products. The white solids were identified as the X^- (X = BPh_4^- for **1a, 3a, 3b,** and **3a,** PF_6^- for **2a**) salts of either protonated *N,N*-bis(2-quinoline)ethane-1,2-diamine (1a), *N,N*-bis(2-quinoline)propane-1,3-diamine (**2a**), *N,N*-bis(6-methyl-2-pyridilmethyl)ethane-1,2-diamine (**3a** and **3b**), or *N,N*-bis(6-methyl-2-pyridilmethyl)propane-1,3-diamine (**4a**), each of which was obtained in 70–85% yields. The CH_2Cl_2-soluble component was shown to consist of 3-methyl-2-butanone-3-disulfide (80–90%; Figures S-33, S-34 in SI), as well as either *tert*-butanol (70–80%, from **1a** to **4a**) or acetophenone (68– 72%, **3b**). The disulfide product may form via a reaction between a highly reactive *tert*-butoxy radical and the thiolate ligand moiety, suggesting that the pentadentate ligands of **1a– 4a** may serve as an internal trapping reagent in these reactions. Identification of the insoluble black precipitate was less conclusive; however, we suspect that this product is likely a manganese oxide of some sort.

Analysis of the anaerobic thermal decay products from **3b** was of particular interest, given that cumene hydroperoxide is well-recognized as a mechanistic probe for homolytic vs heterolytic O–O bond-cleaving pathways. Thermal decay of 1b was previously reported to exclusively produce acetophe-none (68%), as opposed to cumenol (0%), which strongly suggested a homolytic, as opposed to heterolytic, O–O bond-cleaving pathway was involved. With cumeneperoxo-ligated **3b**, we again only observed exclusive formation of acetophenone (72%), as opposed to cumenol. This supports our conclusions based on kinetics, and *suggests that* O*–O bond homolysis is the predominant reaction pathway* for **3b**. In light of the kinetic *trends established* for **3b** vs **1a–4a**, this observation further supports a homolytic O–O bond-cleavage pathway in the thermal decay of **1a–4a**. It is worth noting that ^{t}BuOO$^-$/^{t}BuOOH and CmOO$^-$/CmOOH were not observed even in trace amounts, providing evidence to suggest that homolytic or heterolytic Mn–O bond cleavage is not an

operative process in these systems. To our knowledge, these are the only known Mn(III)–peroxo compounds that decay via homolytic, as opposed to heterolytic, O–O bond cleavage.

Given that Et_3P has been shown to serve as a probe for *tert*-butoxide radicals,[53] we examined reactions between **1a** to **4a** and Et_3P (10 equiv) under anaerobic conditions. Analysis of the final reaction mixture by GC/MS showed a 24% yield of Et_2PO^tBu and 31% yield of Et_3PO. These products are consistent with a decay mechanism involving homolytic O–O bond cleavage, followed by the formation of a *tert*-butoxy radical, as well as a transient Mn(IV)=O. We have been unable to probe or independently synthesize the Mn(IV)=O, most likely because it is highly reactive.

Finally, we sought to determine whether **1a–4a** and **3b** display any reactivity toward exogenous organic molecules. Reactions were examined using a wide variety of substrates including cyclohexane, cyclohexane carboxaldehyde, tetracyano-ethylene, styrene, triphenylphosphine, triethylphosphine, thio-anisole, 1-hydroxy-2,2,6,6-tetramethyl-piperidine (TEMPO-H), dihydroanthracene (DHA), and 2,4-di-*tert*-butylphenol. These reactions were monitored by electronic absorption spectroscopy at 273 and 293 K in a fashion analogous to the kinetics experiments described above. The decay rates of **1a–4a** and **3b** were unperturbed by the presence of these substrates, even at 500-fold excess amounts. Each reaction displayed a zero-order dependence on substrate concentration, suggesting that alkylperoxo **1a–4a** and **3b** are themselves relatively unreactive toward external substrates (Figures S-35–S-49 in SI). Analysis of the final reaction mixtures did, however, show that substrate oxidation occurs. The invariance in thermal decay rates both in the presence and absence of substrates indicates that the reactive oxidant forms following rate-limiting O–O bond cleavage. Since this was not the focus of our study and many of the substrates analyzed could react with either a metal-based or organic radical oxidant, most of these reactions were not pursued further.

Summary and Conclusions

Four new Mn(III)–alkylperoxo complexes were synthesized and structurally and spectroscopically characterized. This extends the number of crystallographically characterized monomeric Mn(III)–peroxo compounds to 10. The ligand backbone of the series described herein was shown to alter metal–ligand distances and modulate electronic properties and the degree of peroxo O–O bond activation. Although not technically bonded, the N-heterocyclic amines were shown to systematically move toward the metal ion upon removal of a methylene unit and alteration of the base (py→quinoline), and this was shown to gradually shift both the electronic absorption energies and associated extinction coefficients. The increased metal ion Lewis acidity caused by elongation of the N-heterocyclic amine Mn···N(3,4) distances was found to shorten the Mn(III)–O(peroxo) bonds and facilitate π(Mn–O) bonding. It was concluded on the basis of a correlation between shifts to the electronic absorption band and peroxo O–O bond lengths that the ligand-centered orbital involved in the π(Mn–O) bond is an antibonding π_v*(O–O) orbital, and this orbital is involved in the high-energy charge transfer transition seen in the electronic spectrum. The peroxo O–O bond was shown to gradually become more activated as the N-heterocyclic amines moved closer to the metal ion, due to decreased shifting of electron density out of the π_v*(O–O) orbital onto the metal (i.e., π-donation). Theoretical calculations support this. An increased interaction with the N-heterocyclic amines would decrease the metal ion Lewis acidity, making it a poor π-acceptor. Theoretical studies showed that the Lewis acidity of the metal ion directly influences the extent of O–O bond activation, with longer O–O bonds occurring in the less Lewis acidic metal complexes. The identity of the ROO^- alkyl substituent was shown to have no effect upon these structural and reactivity trends. Temperature-dependent kinetic parameters for the decay of the compounds

described herein were shown to correlate with the peroxo O-O bond length, consistent with a mechanism involving rate-determining O–O bond cleavage. The products of decay were shown to be consistent with homolytic O–O bond cleavage.

Supplementary Material

Refer to Web version on PubMed Central for supplementary material.

Acknowledgments

J.K. acknowledges the NIH (RO1GM45881-20) for funding. S.D. acknowledges the Max Planck Society for funding, and the Sloan Foundation for a fellowship.

References

1. Cotruvo JA Jr, Stubbe J. Biochemistry. 2010; 49:1297–1309. [PubMed: 20070127]
2. Umena Y, Kawakami K, Shen JR, Kamiya N. Nature. 2011; 473:55–60. [PubMed: 21499260]
3. Oliw EH, Jerneren F, Hoffmann I, Sahlin M, Garscha U. Biochim Biophys Acta. 2011; 1811:138–147. [PubMed: 21167311]
4. Perry JJP, Hearn AS, Cabelli DE, Nick HS, Tainer JA, Silverman DN. Biochemistry. 2009; 48:3417–3424. [PubMed: 19265433]
5. Boal AK, Cotruvo JA Jr, Stubbe J, Rosenzweig AC. Science. 2010; 329:1526–1530. [PubMed: 20688982]
6. Barnese K, Sheng Y, Stich T, Gralla EB, Britt RD, Cabelli D, Valentine JS. J Am Chem Soc. 2010; 132:12525–12527. [PubMed: 20726524]
7. Armstrong FA. Philos Trans R Soc London, Ser B. 2008; 363:1263–1270. [PubMed: 17971329]
8. Emerson JP, Kovaleva EG, Farquhar ER, Lipscomb JD, Que L Jr. Proc Natl Acad Sci U S A. 2008; 105:7347–7352. [PubMed: 18492808]
9. McEvoy JP, Brudvig GW. Chem Rev. 2006; 106:4455–4483. [PubMed: 17091926]
10. Hearn AS, Stroupe ME, Cabelli DE, Lepock JR, Tainer JA, Nick HS, Silverman DN. Biochemistry. 2001; 40:12051–12058. [PubMed: 11580280]
11. Jackson TA, Karapetian A, Miller AF, Brunold TC. Biochemistry. 2005; 44:1504–1520. [PubMed: 15683235]
12. Miller AF. Curr Opin Chem Biol. 2004; 8:162–168. [PubMed: 15062777]
13. Yachandra VK, Sauer K, Klein MP. Chem Rev. 1996; 96:2927–2950. [PubMed: 11848846]
14. Bull C, Niederhoffer EC, Yoshida T, Fee JA. J Am Chem Soc. 1991; 113:4069–4076.
15. Shook RL, Gunderson WA, Greaves J, Ziller JW, Hendrich MP, Borovik AS. J Am Chem Soc. 2008; 130:8888–8889. [PubMed: 18570414]
16. Murphy A, Stack DTP. J Mol Catal A: Chem. 2006; 251:78–88.
17. Shook RL, Peterson SM, Greaves J, Moore C, Rheingold AL, Borovik AS. J Am Chem Soc. 2011; 133:5810–5817. [PubMed: 21425844]
18. Goldsmith CR, Cole AP, Stack TDP. J Am Chem Soc. 2005; 127:9904–9912. [PubMed: 15998097]
19. Betley TA, Surendranath Y, Childress MV, Alliger GE, Fu R, Cummins CC, Nocera DG. Philos Trans R Soc London, Ser B. 2008; 363:1293–1303. [PubMed: 17971328]
20. Lewis NS, Nocera DG. Proc Natl Acad Sci U S A. 2006; 103:15729–15735. [PubMed: 17043226]
21. Zhang Y, Stubbe J. Biochemistry. 2011; 50:5615–5623. [PubMed: 21561096]
22. Skulan AJ, Brunold TC, Baldwin J, Saleh L, Bollinger JM Jr, Solomon EI. J Am Chem Soc. 2004; 126:8842–8855. [PubMed: 15250738]
23. Clausen J, Junge W. Nature. 2004; 430:480–483. [PubMed: 15269775]
24. Hamberg M, Su C, Oliw E. J Biol Chem. 1998; 273:13080–13088. [PubMed: 9582346]

25. Skrzypczak-Jankun E, Bross RA, Carroll RT, Dunham WR, Funk MO. J Am Chem Soc. 2001; 123:10814–10820. [PubMed: 11686682]
26. Kovaleva EG, Lipscomb JD. Science. 2007; 316:453–456. [PubMed: 17446402]
27. Emerson JP, Kovaleva EG, Farquhar eR, Lipscomb JD, Que L Jr. Proc Natl Acad Sci U S A. 2008; 105:7347–7352. [PubMed: 18492808]
28. McGarrigle EM, Gilheany DG. Chem Rev. 2005; 105:1536–1602.
29. Boisvert L, Goldberg KI. Acc Chem Res. 2012; 45:899–910. [PubMed: 22578038]
30. Zhang C, Xu Z, Shen T, Wu G, Zhang L, Jiao N. Org Lett. 2012; 14:2362–2365. [PubMed: 22536981]
31. Brinksma J, Hage R, Kerschner JL, Feringa BL. Chem Commun. 2000:537–538.
32. Coggins MK, Kovacs JA. J Am Chem Soc. 2011; 133:12470–12473. [PubMed: 21776951]
33. Geiger RA, Wijeratne G, Day VW, Jackson TA. Eur J Inorg Chem. 2012; 10:1598–1608.
34. Annaraj J, Cho J, Lee YM, Kim SY, Latifi R, de Visser SP, Nam W. Angew Chem, lnt Ed. 2009; 48:4150–4153.
35. Geiger RA, Chattopadhyay S, Day VW, Jackson TA. J Am Chem Soc. 2010; 132:2821–2831. [PubMed: 20136141]
36. Geiger RA, Leto DF, Chattopadhyay S, Dorlet P, Anxolabéhère-Mallart E, Jackson TA. Inorg Chem. 2011; 50:10190–10203. [PubMed: 21875042]
37. Hearn AS, Tu CK, Nick HS, Silverman DN. J Biol Chem. 1999; 274:24457–24460. [PubMed: 10455106]
38. Seo MS, Kim JY, Annaraj J, Kim Y, Lee YM, Kim SJ, Nam W. Angew Chem, lnt Ed. 2007; 46:377–380.
39. Bossek U, Weyhermuller T, Wieghardt K, Nuber B, Weiss J. J Am Chem Soc. 1990; 112:6387–6388.
40. Groni S, Dorlet P, Blain G, Bourcier S, Guillot R, Anxolabéhère-Mallart E. Inorg Chem. 2008; 47:3166–3172. [PubMed: 18370381]
41. VanAtta RB, Strouse CE, Hanson LK, Valentine JS. J Am Chem Soc. 1987; 109:1425–1434.
42. Kitajima N, Komatsuzaki H, Hikichi S, Osawa M, Morooka Y. J Am Chem Soc. 1994; 116:11596–11597.
43. Singh UP, Sharma AK, Hikichi S, Komatsuzaki H, Morooka Y, Akita M. Inorg Chim Acta. 2006; 359:4407–4411.
44. Liu SY, Soper JD, Yang JY, Rybak-Akimova EV, Nocera DG. Inorg Chem. 2006; 45:7572–7574. [PubMed: 16961343]
45. Namuswe F, Hayashi T, Jiang Y, Kasper GD, Narducci Sarjeant AA, Moënne-Loccoz P, Goldberg DP. J Am Chem Soc. 2010; 132:157–167. [PubMed: 20000711]
46. Lehnert N, Ho RYN, Que LJ, Solomon EI. J Am Chem Soc. 2001; 123:12802–12816. [PubMed: 11749538]
47. Kitagawa T, Dey A, Lugo-Mas P, Benedict J, Kaminsky W, Solomon E, Kovacs JA. J Am Chem Soc. 2006; 128:14448–14449. [PubMed: 17090014]
48. Shan X, Rohde JU, Koehntop KD, Zhou Y, Bukowski MR, Costas M, Fujisawa K, Que L Jr. Inorg Chem. 2007; 46:8410–8417. [PubMed: 17764172]
49. Lehnert N, Ho RYN, Que LJ, Solomon EI. J Am Chem Soc. 2001; 123:8271–8290. [PubMed: 11516278]
50. Denisov IG, Makris TM, Sligar SG, Schlichting I. Chem Rev. 2005; 105:2253–2277. [PubMed: 15941214]
51. Que L, Tolman WB. Nature. 2008; 455:333–340. [PubMed: 18800132]
52. Walling C, Buckler SA. J Am Chem Soc. 1955; 77:6032–6038.
53. DiPasquale AG, Hrovat DA, Mayer JM. Organometallics. 2006; 25:915–924. [PubMed: 18725968]
54. Coggins MK, Toledo S, Shaffer E, Kaminsky W, Shearer J, Kovacs JA. Inorg Chem. 2012; 51:6633–6644. [PubMed: 22642272]
55. Live DH, Chan SI. Anal Chem. 1970; 42:791.

56. Van Geet AL. Anal Chem. 1968; 40:2227–2229.
57. Neese, F. ORCA-an ab initio,density functional and semi-empirical program package, Version 2.7. University of Bonn; Bonn, Germany: 2010.
58. Roemelt M, Beckwith MA, Duboc C, Collomb MN, Neese F, DeBeer S. Inorg Chem. 2012; 51:680–687. [PubMed: 22145735]
59. Buhl M, Kabrede H. J Chem Theory Comput. 2006; 2:1282–1290.
60. Lenthe, Ev; Baerends, EJ.; Snijders, JG. J Chem Phys. 1993; 99:4597.
61. van Wullen C. J Chem Phys. 1998; 109:392.
62. Weigend F, Ahlrichs R. Phys Chem Chem Phys. 2005; 7:3297. [PubMed: 16240044]
63. Klamt A, Schüürmann G. J Chem Soc, Perkin Trans. 1993:799.
64. Tao J, Perdew JP, Staroverov VN, Scuseria GE. Phys Rev Lett. 2003; 91:146401. [PubMed: 14611541]
65. Tao J, Perdew JP, Staroverov VN, Scuseria GE. Phys Rev Lett. 2004; 120:6898–6911.
66. Waasmaier D, Kirfel A. Acta Crystallogr A. 1995; 51:416.
67. Shannon RD. Acta Crystallogr. 1976; A32:751–767.
68. Kitajima N, Katayama T, Fujisawa K, Iwata Y, Moro-oka Y. J Am Chem Soc. 1993; 115:7872–7873.
69. Hikichi S, Komatsuzaki H, Akita M, Moro-oka Y. J Am Chem Soc. 1998; 120:4699–4710.
70. Chavez FA, Mascharak PK. Acc Chem Res. 2000; 33:539–545. [PubMed: 10955984]
71. Chavez FA, Rowland JM, Olmstead MM, Mascharak PK. J Am Chem Soc. 1998; 120:9015.
72. Komatsuzaki H, Sakamoto N, Satoh M, Hikichi S, Akita M, Moro-oka Y. Inorg Chem. 1998; 37:6554–6555. [PubMed: 11670782]
73. Henson MJ, Vance MA, Zhang CX, Liang HC, Karlin KD, Solomon EI. J Am Chem Soc. 2003; 125:5186–5192. [PubMed: 12708870]
74. Hatcher LQ, Vance MA, Narducci Sarjeant AA, Solomon EI, Karlin KD. Inorg Chem. 2006:3004–3013. [PubMed: 16562956]
75. Hatcher LQ, Lee DH, Vance MA, Milligan AE, Sarangi R, Hodgson KO, Hedman B, Solomon EI, Karlin KD. Inorg Chem. 2006; 45:10055–10057. [PubMed: 17140210]
76. Lee Y, Park GY, Lucas HR, Vajda PL, Kamaraj K, Vance MA, Milligan AE, Woertink JS, Siegler MA, Narducci Sarjeant AA, Zakharov LN, Rheingold AL, Solomon EI, Karlin KD. Inorg Chem. 2009; 48:11297–11309. [PubMed: 19886646]
77. Roelfes G, Vrajmasu V, Chen K, Ho RYN, Rohde JU, Zondervan C, Crois RM, Schudde EP, Lutz M, Spek AL, Hage R, Feringa BL, Munck E, Que L Jr. Inorg Chem. 2003; 42:2639–2653. [PubMed: 12691572]
78. Cho J, Sarangi R, Nam W. Acc Chem Res. 2012; 45:1321–1330. [PubMed: 22612523]
79. Solomon EI, Brunold TC, Davis MI, Kemsley JN, Lee SK, Lehnert N, Neese F, Skulan AJ, Yang YS, Zhou J. Chem Rev. 2000; 100:233–349.
80. Lugo-Mas P, Dey A, Xu L, Davin SD, Benedict J, Kaminsky W, Hodgson KO, Hedman B, Solomon EI, Kovacs JA. J Am Chem Soc. 2006; 128:11211–11221. [PubMed: 16925440]
81. This shift in peroxo contribution is diminished by a shift in contributions from the thiolate sulfur, which is predicted to rise from ~5.7% to ~11%.
82. Halpern. J Bull Chem Soc Jpn. 1988; 61:13–15.
83. Liu L, Guo QX. Chem Rev. 2001; 101:673–696. [PubMed: 11712500]
84. Jones PG, Kirby AJ. J Am Chem Soc. 1984; 106:6207–6212.
85. Mayer JM. Acc Chem Res. 1998; 31:441–450.
86. Jensen MP, Mairata i Payeras A, Fielder AT, Costas M, Kaizer J, Stubna A, Munck E, Que L Jr. Inorg Chem. 2007; 46:2398–2408. [PubMed: 17326618]
87. Chin DH, La Mar GN, Balch AL. J Am Chem Soc. 1980; 102:4344–4350.

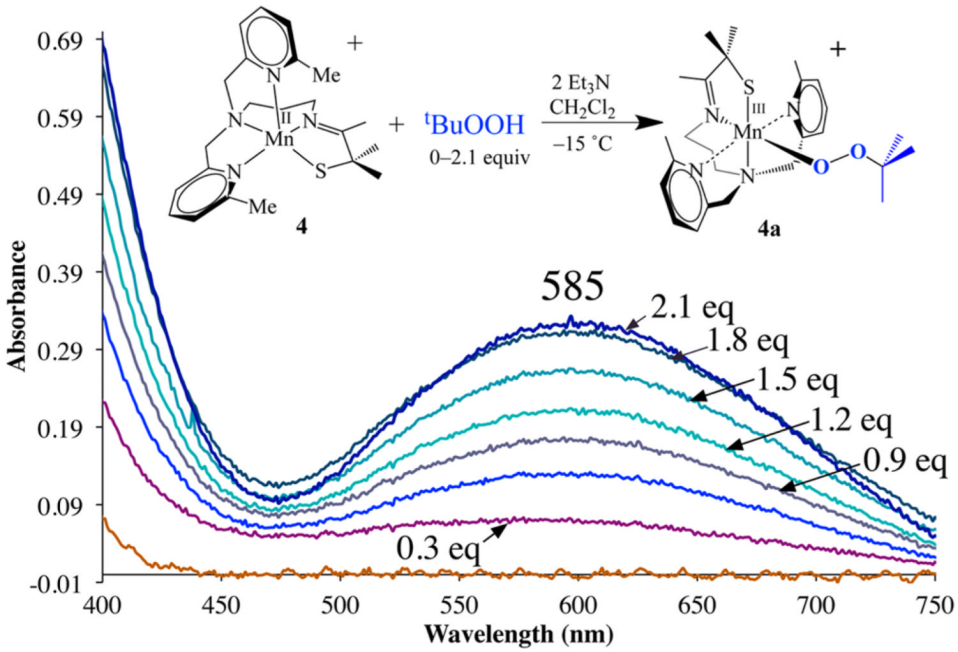

Figure 1.

Titration of 0–2.1 equiv of ^{t}BuOOH (in 0.3-equiv aliquots) to a CH_2Cl_2 solution $[Mn^{II}(S^{Me2}N_4(6\text{-Me-DPPN}))](BPh_4)$ (4; 2.2 mM), in the presence of 2 equiv of Et_3N, at −15 °C as monitored by visible absorption spectroscopy.

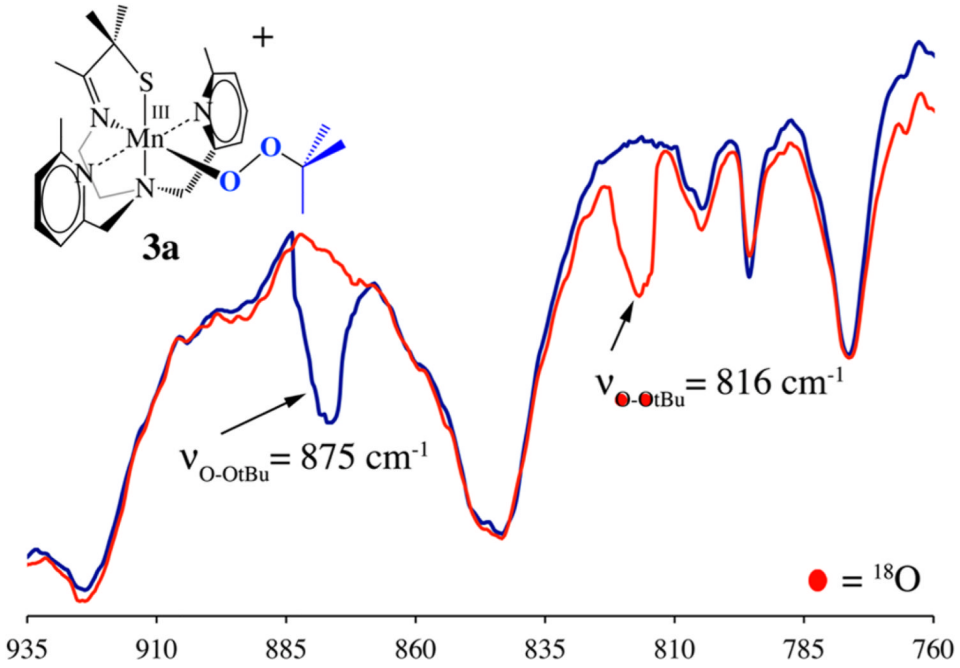

Figure 2.
FT-IR (nujol mull) of metastable $[Mn^{III}(S^{Me2}N_4(6\text{-Me-DPEN}))(^{16}O^{16}O^tBu)]^+$ (**3a**; blue) vs metastable $[Mn^{III}(S^{Me2}N_4(6\text{-Me-DPEN}))(^{18}O^{18}O^tBu)]^+$ (**3a**; red).

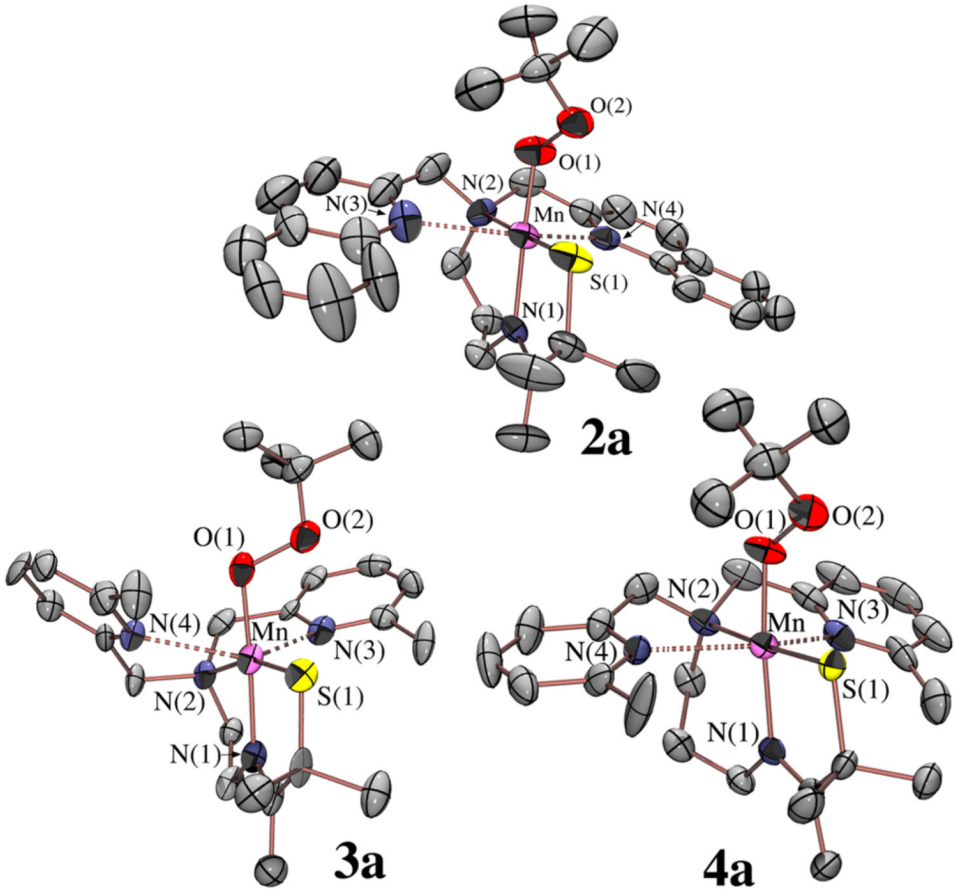

Figure 3.

ORTEP diagrams (50% probability ellipsoids) of $[Mn^{III}(S^{Me2}N_4(QuinoPN))(OO^tBu)]^+$ (**2a**), $[Mn^{III}(S^{Me2}N_4(6\text{-Me-DPEN}))(OO^tBu)]^+$ (**3a**), and $[Mn^{III}(S^{Me2}N_4(6\text{-Me-DPPN}))\text{-}(OO^tBu]^+$ (**4a**) showing exceedingly long Mn··N(3,4) interactions (Table 3) as dashed lines. Hydrogen atoms, counterions, and solvents of crystallization have been omitted.

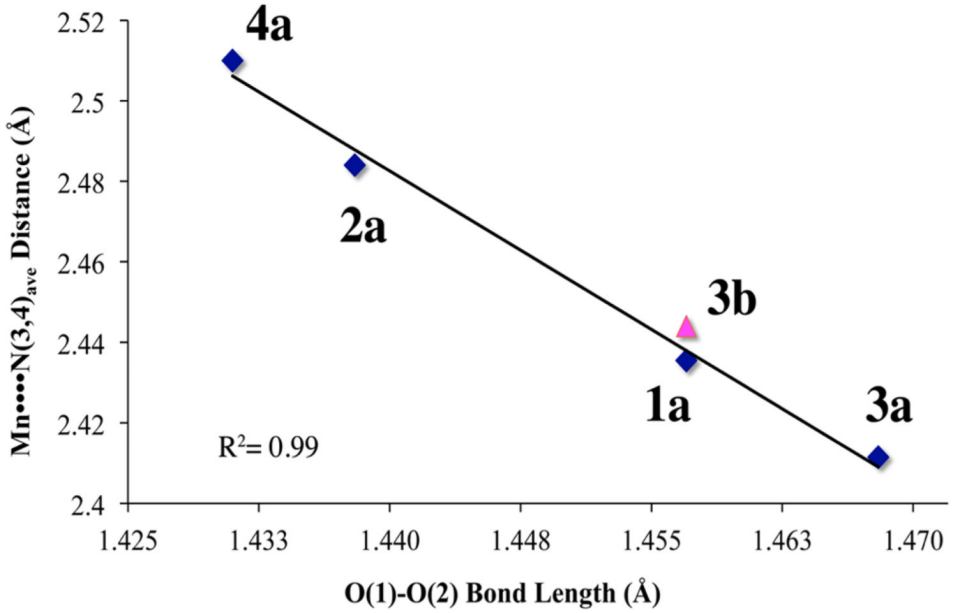

Figure 4.

Plot of O(1)–O(2) bond length (Å) vs Mn(III)–$N(3,4)_{avg}$ distance (Å) for Et-linked (**1a**, **3b**, and **3a**), and Pr-linked (**2a** and **4a**) structures. Data for [$Mn^{III}(S^{Me2}N_4$(6-Me-DPEN))(OOCm](BPh_4) (**3b**) is represented by the pink triangle and is not included in the linear fit correlation coefficient (R^2).

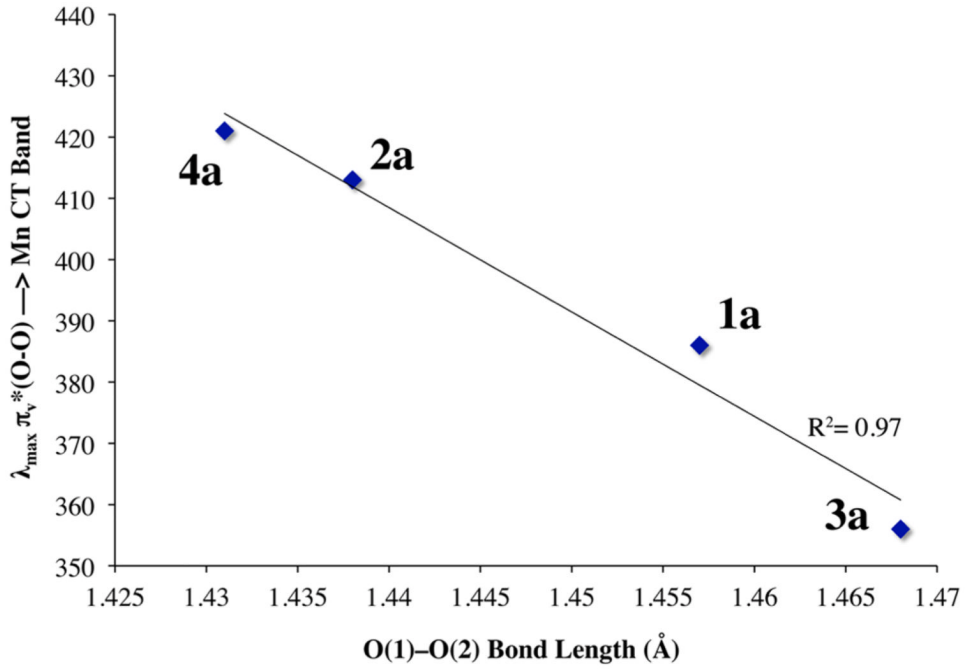

Figure 5.
Plot of O(1)–O(2) bond length vs λ_{max} (nm) for the high-energy absorption bands displayed by **1a–4a**.

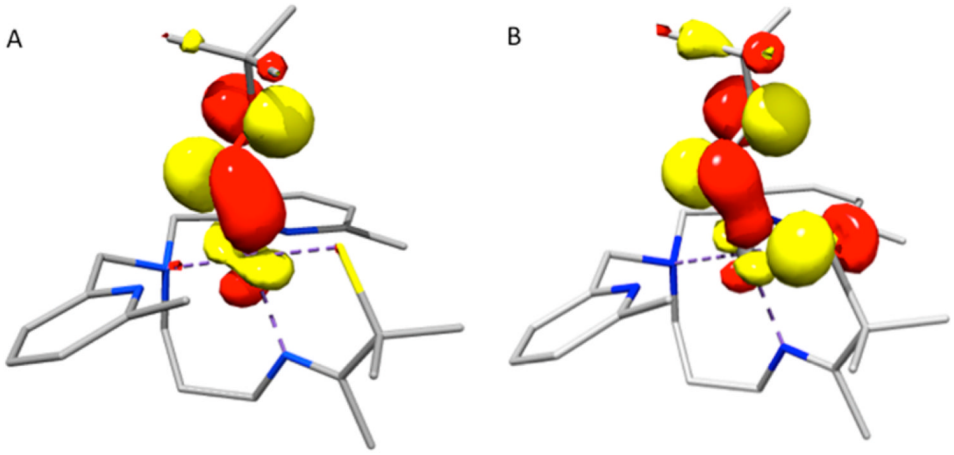

Figure 6.

Bonding π(Mn–O) orbitals (isovalue = 0.035) for alkylperoxo compound **4a** at the O–O = 1.2 Å (A) and 1.5 Å (B) bond limits. Both involve an antibonding peroxo π_v*(O–O) orbital interacting with a Mn d_{xz} orbital. The Mn contribution drops from 24.2% (A) to 11.4% (B) with increasing O–O bond length. The change in Mn contribution is largely compensated by donation from the sulfur π_p orbital (0.2% at 1.2 Å vs 11.9% at 1.5 Å).

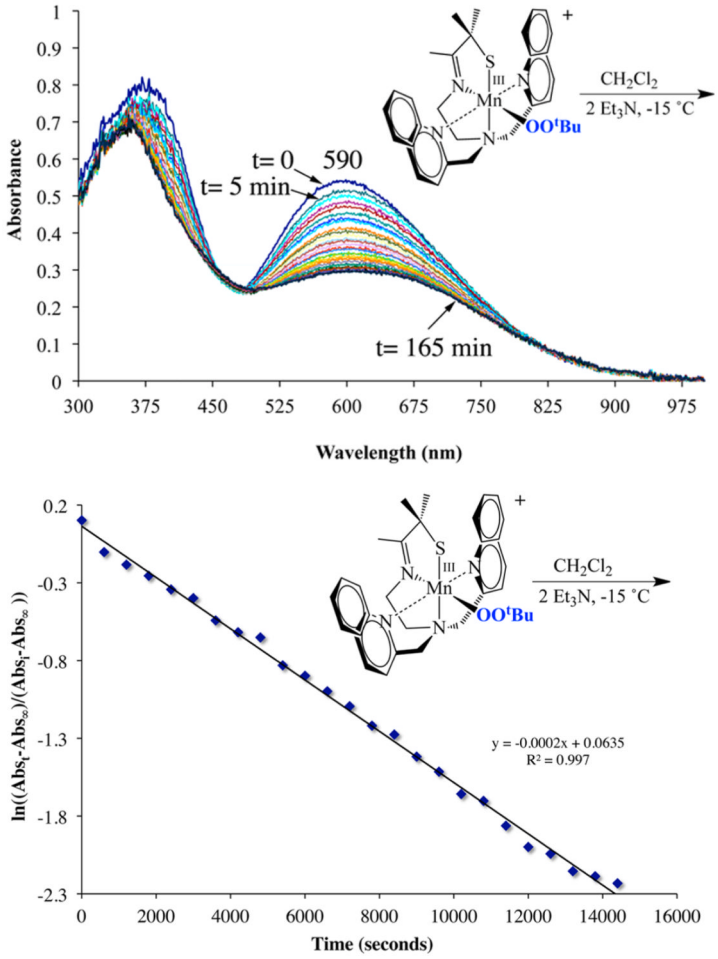

Figure 7.

Electronic absorption spectra displaying the thermal decay of **2a** in CH_2Cl_2 at 258 K with individual scans representing 5-min intervals (top). Kinetics plot of $\ln[(A_t - A_\infty)/(A_i - A_\infty)]$ vs time for the thermal decay of **2a** in CH_2Cl_2 at 258 K (bottom).

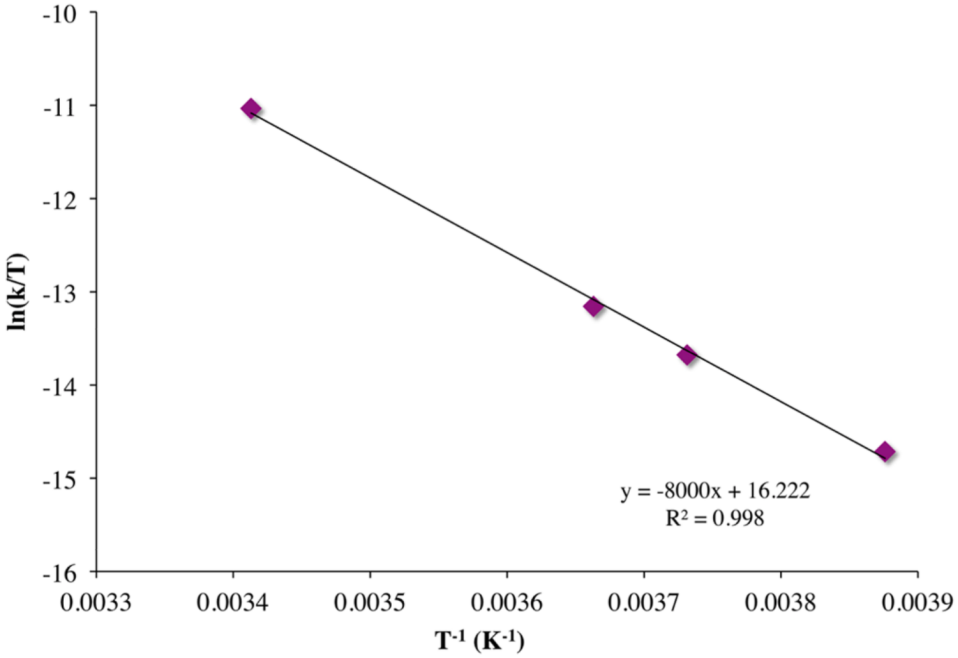

Figure 8.

Eyring plot from the variable-temperature decay kinetics data for [$Mn^{III}(S^{Me2}N_4$(6-Me-DPPN))(OO^tBu](BPh_4) (**4a**) in CH_2Cl_2.

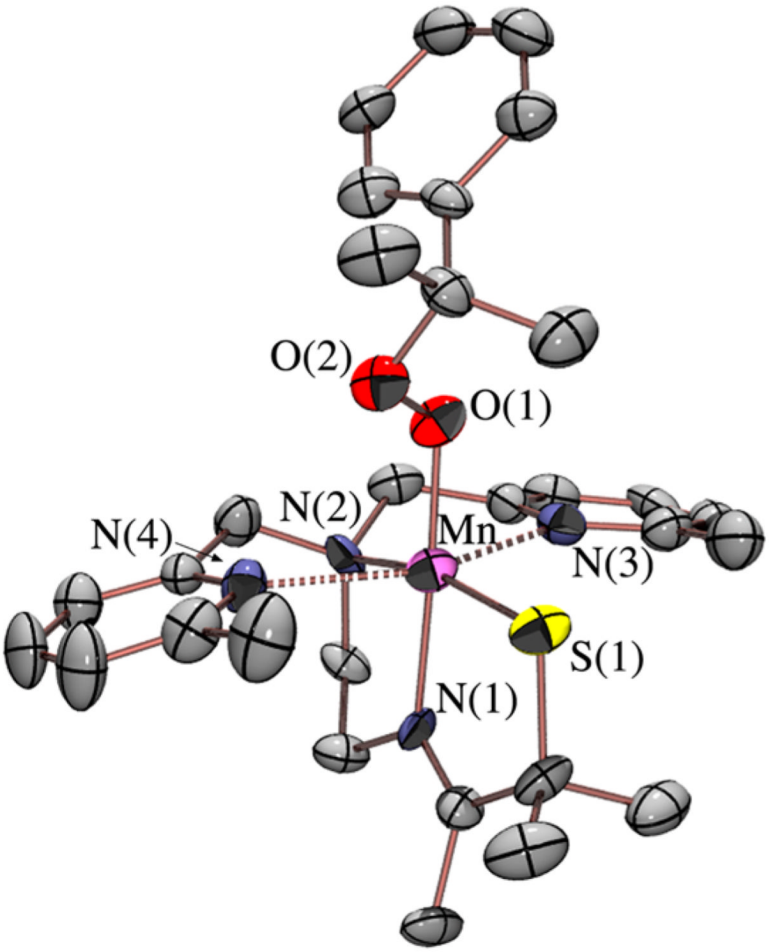

Figure 9.

ORTEP diagram (50% probability ellipsoids) of $[Mn^{III}(S^{Me2}N_4(6\text{-Me-DPEN}))(OOCm)]^+$ (**3b**) showing exceptionally long Mn···N(3,4) intgeractions as dashed lines. Hydrogen atoms, counterions, and solvent of crystallization have been omitted for clarity.

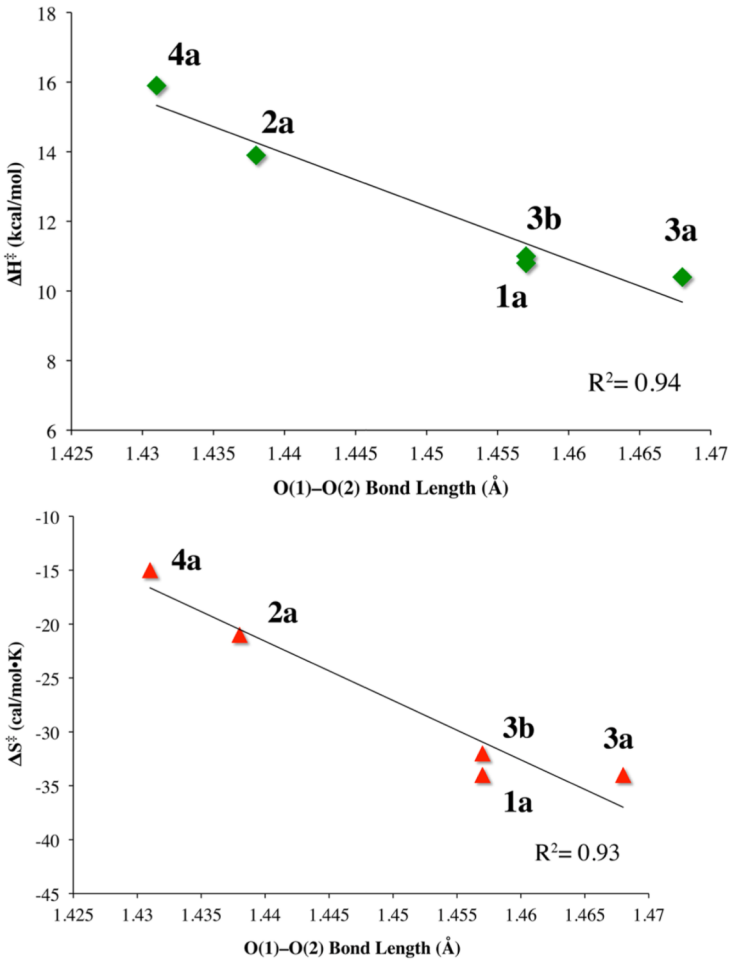

Figure 10.
Plot of activation enthalpy (kcal/mol) (top) and activation entropy (cal/mol·K) (bottom) vs O(1)–O(2) bond length (Å).

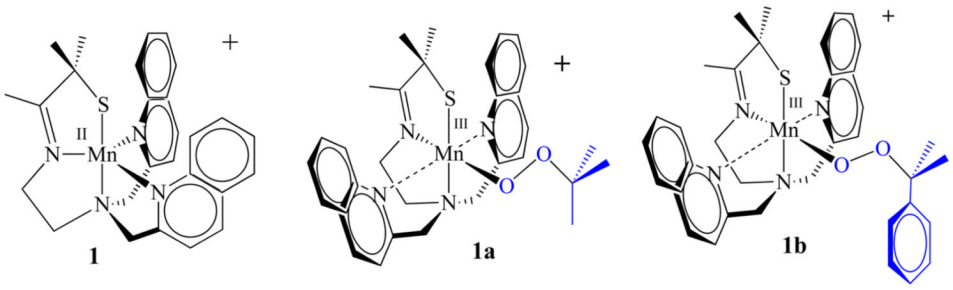

Scheme 1.

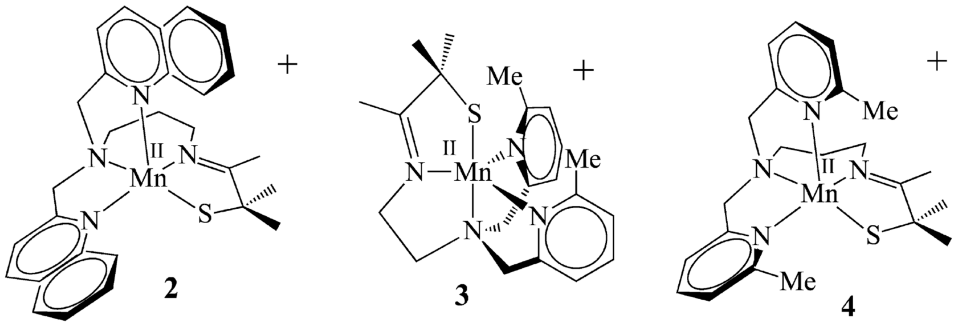

Scheme 2.

Table 1

Crystal Data for $[Mn^{III}(S^{Me2}N_4(QuinoPN))(OO^tBu)](PF_6)\cdot C_5H_{12}$ (2a), $[Mn^{III}(S^{Me2}N_4(6\text{-}Me\text{-}DPEN))(OO^tBu)](BPh_4)$ (3a), $[Mn^{III}(S^{Me2}N_4(6\text{-}Me\text{-}DPEN))(OOCm](BPh_4)$ (3b), $[Mn^{III}(S^{Me2}N_4(6\text{-}Me\text{-}DPPN))(OO^tBu](BPh_4)\cdot Et_2O$ (4a)

	2a	3a	3b	4a
formula	$C_{69}H_{92}F_{12}Mn_2N_8P_2S_2$	$C_{53}H_{68}BMnN_4O_3S$	$C_{56}H_{64.65}BCl_{1.34}Mn\ N_4O_{2.33}S$	$C_{50}H_{60}BMnN_4O_2S$
MW	1561.45	906.92	976.36	846.83
T, *K*	100(2)	100(2)	100(2)	100(2)
unit cell[a]	monoclinic	orthorhombic	triclinic	triclinic
a, Å	10.5559(8)	17.265(2)	12.8928(18)	9.5420(7)
b, Å	14.0937(10)	25.499(3)	14.433(2)	14.5846(11)
c, Å	23.9583(16)	11.2048(14)	15.069(3)	16.4547(13)
α, deg	90	90	71.085(10)	77.689(4)
β, deg	94.560(4)	90	77.463(10)	83.682(4)
γ, deg	90	90	82.463(9)	78.144(4)
V, Å^3	3553.0(4)	4932.7(11)	2583.7(7)	2184.3(3)
Z	2	4	2	2
d(calc), g/cm^3	1.460	1.221	1.255	1.288
space group	$P2_1/n$	$Pna2_1$	$P\bar{1}$	$P\bar{1}$
R^b	0.0688	0.0696	0.1004	0.0667
$R_w{}^c$	0.2088	0.1246	0.2391	0.1786
GOF	1.013	1.000	0.952	1.008

[a] In all cases: Mo Kα(λ = 0.71070 Å) radiation.

[b] $R = \Sigma||F_O| - |F_C||/\Sigma|F_O|$.

[c] $R_W = [\Sigma w(|F_O| = |F_C|)^2/\Sigma wF_O{}^2]^{1/2}$, where $w^{-1} = [\sigma_{count}{}^2 + (0.05F^2)^2]/4F^2$.

Table 2

Electronic Absorption and IR Parameters for Alkylperoxo Compounds 1a−4a in CH_2Cl_2 at 258 K

	λ_{max} (ε, cm^{-1} M^{-1}) nm	λ_{max} (ε, cm^{-1} M^{-1}) nm	ν_{O-O} ($\Delta^{18}O$) (cm^{-1}) nm
$[Mn^{III}(S^{Me2}N_4$(6-Me-DPPN))$(OO^tBu)](BPh_4)$ (**4a**)[a]	420(240)	585(320)	893(58)
$[Mn^{III}(S^{Me2}N_4$(QuinoPN))$(OO^tBu)](PF_6)$ (**2a**)	415(510)	590(465)	895(64)
$[Mn^{III}(S^{Me2}N_4$(QuinoEN))$(OO^tBu)](BPh_4)$ (**1a**)	385(640)	590(465)	888(57)
$[Mn^{III}(S^{Me2}N_4$(6-Me-DPEN))$(OO^tBu)](BPh_4)$ (**3a**)	355(1060)	600(575)	875(59)

[a]Arranged in order of decreasing λ_{max} in the near UV region.

Table 3

Selected Bond Distances (Å) and Bond Angles (deg) for $[Mn^{III}(S^{Me2}N_4(QuinoEN))(OO^tBu)](BPh_4)$ (1a), $[Mn^{III}(S^{Me2}N_4(QuinoPN))(OO^tBu)](PF_6)\cdot$pentane (2a), $[Mn^{III}(S^{Me2}N_4(6\text{-Me-DPEN}))(OO^tBu)](BPh_4)$ (3a), $[Mn^{III}(S^{Me2}N_4(6\text{-Me-DPEN}))(OOCm](BPh_4)$ (3b), and $[Mn^{III}(S^{Me2}N_4(6\text{-Me-DPPN}))(OO^tBu](BPh_4)\cdot Et_2O$ (4a)

	1a	2a	3a	3b	4a
Mn–S(1)	2.270(3)	2.2693(15)	2.241(3)	2.268(2)	2.2603(13)
Mn–N(1)	2.034(7)	2.046(4)	2.015(8)	2.018(5)	2.061(4)
Mn–N(2)	2.173(7)	2.182(4)	2.163(7)	2.145(5)	2.178(4)
Mn–N(3)	2.349(7)	2.450(5)	2.354(8)	2.499(6)	2.517(4)
Mn–N(4)	2.522(8)	2.518(5)	2.471(7)	2.389(5)	2.504(4)
Mn–O(1)	1.861(5)	1.840(4)	1.853(6)	1.848(4)	1.843(3)
O(1)–O(2)	1.457(7)	1.438(5)	1.468(7)	1.457(5)	1.431(5)
Mn··O(2)	2.714	2.861	2.769	2.756	2.901
Mn–O(1)–O(2)	109.2(4)	121.1(3)	112.4(4)	112.4(3)	124.2(3)
O(1)–Mn–N(1)	175.4(3)	176.12(16)	175.7(3)	176.9(2)	174.27(15)
S(1)–Mn–N(2)	163.1(2)	177.62(13)	162.6(2)	164.95(14)	176.78(11)
O(1)–Mn–S(1)	97.5(2)	93.69(12)	94.9(2)	99.92(14)	91.79(11)
O(1)–Mn–N(2)	97.9(3)	84.16(17)	102.2(3)	94.23(19)	85.02(14)
S(1)–Mn–N(1)	82.3(2)	82.44(12)	83.6(2)	83.11(16)	83.32(11)
S(1)–Mn–N(4)	105.6(3)	108.98(14)	109.13(18)	107.23(16)	108.32(10)
Mn–O(1)–O(2)–C	139.51°	131.85°	163.69	142.22°	126.68°

Table 4

Selected metrical, spectroscopic, and kinetic data for $[Mn^{III}(S^{Me2}N_4(QuinoEN))(OO^tBu)](BPh_4)$ (1a), $[Mn^{III}(S^{Me2}N_4(QuinoPN))(OO^tBu)](PF_6)$·pentane (2a), $[Mn^{III}(S^{Me2}N_4(6\text{-Me-DPEN}))(OO^tBu)](BPh_4)$ (3a), and $[Mn^{III}(S^{Me2}N_4(6\text{-Me-DPPN}))(OO^tBu](BPh_4)\cdot Et_2O$ (4a)

	ligand backbone	$Mn\cdots N(3,4)_{avg}$ (Å)	O–O (Å)	λ_{max} (ε, $cm^{-1}\ M^{-1}$) nm	$\nu_{O-O}(\Delta^{18}O)$ (cm^{-1})	$\Delta H^{\ddagger}$ (kcal/mol)
4a	Pr	2.510	1.431(5)	420(240)	893(58)	15.9(5)
2a	Pr	2.484	1.438(5)	415(510)	895(64)	13.8(4)
1a	Et	2.435	1.457(7)	385(640)	888(57)	11.6(4)
3a	Et	2.411	1.468(7)	355(1060)	875(59)	10.5(3)

Table 5

Kinetics data for the Decay of Alkylperoxos $[Mn^{III}(S^{Me2}N_4(QuinoEN))(OO^tBu)]$ (BPh_4) (1a), $[Mn^{III}(S^{Me2}N_4(QuinoPN))(OO^tBu)](PF_6)$ (2a), $[Mn^{III}(S^{Me2}N_4(6\text{-Me-DPEN}))$ $(OO^tBu)](BPh_4)$ (3a), $[Mn^{III}(S^{Me2}N_4(6\text{-Me-DPEN}))(OOCm](BPh_4)$ (3b), $[Mn^{III}(S^{Me2}N_4(6\text{-Me-DPPN}))$ $(OO^tBu](BPh_4)$ (4a)

	3a	1a	3b	2a	4a
k_1 (s^{-1}), 293 K	0.00278	0.00189	0.00257	0.0051	0.00473
k_1 (s^{-1}), 273 K	0.00101	0.00043	0.00079	0.001	0.000528
k_1 (s^{-1}), 268 K	0.000623	0.00033	0.000698	0.000559	0.000308
k_1 (s^{-1}), 258 K	0.000205	0.00013	0.00015	0.000172	0.000105
$\Delta H^{\ddagger}$ (kcal/mol)	10.4	10.8	11.0	13.9	15.9
$\Delta S^{\ddagger}$ (cal/mol·K)	−34	−34	−32	−21	−15